

Spatially Resolved Observations of the Galactic Center Source, IRS 21

A. Tanner, A. M. Ghez¹, M. Morris and E. E. Becklin

UCLA Department of Physics and Astronomy, Los Angeles, CA 90095-1562

A. Cotera

Steward Observatory, University of Arizona, Tucson, AZ 85721

M. Ressler, M. Werner

Jet Propulsion Lab, 169-327, 4800 Oak Grove Drive, Pasadena, CA, 91109

P. Wizinowich

W.M. Keck Observatory, 65-1120 Mamalahoa Hwy., Kamuela, HI 96743

ABSTRACT

We present diffraction-limited 2-25 μm images obtained with the W. M. Keck 10-m telescopes that spatially resolve the cool source, IRS 21, one of a small group of enigmatic objects in the central parsec of our Galaxy that have eluded classification. Modeled as a Gaussian, the azimuthally-averaged intensity profile of IRS 21 has a half-width half-maximum (HWHM) size of 650 ± 80 AU at 2.2 μm and an average HWHM size of 1600 ± 200 AU at mid-infrared wavelengths. These large apparent sizes imply an extended distribution of dust. The mid-infrared color map indicates that IRS 21 is a self-luminous source rather than an externally heated dust clump as originally suggested. The spectral energy distribution has distinct near- and mid-infrared components. A simple radiative transfer code, which simultaneously fits the near- and mid-infrared photometry and intensity profiles, supports a model in which the near-infrared radiation is scattered and extincted light from an embedded central source, while the mid-infrared emission is from thermally re-radiating silicate dust. We argue that IRS 21 (and by analogy the other luminous sources along the Northern Arm) is a massive star experiencing rapid mass loss and plowing through the Northern Arm, thereby generating a bow shock, which is spatially resolved in our observations.

Subject headings: Galaxy: center — infrared: stars

¹Also affiliated with UCLA Institute for Geophysics and Planetary Physics

1. Introduction

IRS 21 is one of the most distinctive objects within the central parsec of our Galaxy, a region abounding in extraordinary objects. Within the central parsec, IRS 21 has the largest K-band [$2.2\ \mu\text{m}$] polarization, $\sim 10\%$ (Ott et al. 1999; Eckart et al. 1995), and is one of the few objects to have both extremely red colors ($H-K > 3$) and a featureless K-band spectrum (Blum, Sellgren, & Depoy 1996; Krabbe et al. 1995; Ott et al. 1999). Gezari et al. (1985) initially identified IRS 21 in 8.3 and $12.4\ \mu\text{m}$ images as a strong mid-infrared peak located along the Northern Arm, a tidal stream of dust and gas (Gezari et al. 1985, Lacy et al. 1980) that is infalling towards and orbiting around the supermassive ($M_{BH} \sim 2.6 \times 10^6 M_{\odot}$) central black hole Sgr A* (Genzel et al. 1996, 2000; Ghez et al. 1998, 2000). Along the Northern Arm, there are a handful of other similarly strong mid-infrared sources ($L \sim 10^{4-5} L_{\odot}$), including IRS 1, 2, 5, 8, and 10 (nomenclature from Becklin et al. 1978), which will be referred to collectively as the “Northern Arm Sources.” In addition to having similar mid-infrared luminosities, these objects share the characteristics of featureless near-infrared spectra² and relatively cool colors. Although there are only a few other comparably luminous objects in the central parsec, IRS 21 and the other Northern Arm sources have eluded definitive classification.

Initially, Gezari et al. (1985) suggested that IRS 21 is an externally heated, high-density dust clump. Several other classifications have also been proposed since then, including an embedded early-type star and a protostar (Krabbe et al. 1995; Blum et al. 1996; Ott et al. 1999). The most recent analysis of this object was presented by Ott et al., who marginally resolved IRS 21 in $2.2\ \mu\text{m}$ images with an angular resolution of $0''.15$. Although they do not report a physical size, they use the featureless, red spectra, along with the relative orientations of the 2 and $12\ \mu\text{m}$ polarization angles, to argue that IRS 21 is a recently formed star still embedded in its protostellar dust shell.

The suggestion that IRS 21 is a newly formed object would favor a scenario wherein all the Northern Arm sources originated within the Northern Arm. At present, however, establishing a dynamical association between the gas and the infrared sources is not possible, as the V_{LSR} for these sources has not been determined explicitly; their near-infrared spectra are featureless, and the proper motion measurements of the stars and gas at their position are insufficient. There is, however, a serious problem with the protostellar hypothesis even without the velocity data; the dynamical timescale for the gas along the Northern Arm is as short as 10^4 years (Lo and Claussen 1983), substantially shorter than the timescale for

²Only three of the Northern Arm sources, IRS 21, 1W and 10W, have measured K-band spectra (Krabbe et al. 1995).

star formation. Therefore, the Northern Arm sources, if they are young, would have to have formed, or to have begun forming, prior to the infall of the Northern Arm. In this case one would not expect the stars to still be embedded in the gas of the Northern Arm given that the newborn stars would have immediately started following ballistic orbits while the gas in which they formed is subject to strong, additional, non-gravitational forces. Unlike the stars, the gas is subject to forces such as: 1) magnetic forces in the strongly magnetized medium (Aitken et al. 1998), 2) the ram pressure of the strong stellar winds emanating from the central cluster of luminous emission-line stars (Krabbe et al. 1995; Paumard et al. 2001), 3) the radiation pressure from these same stars, 4) the gas dynamical pressures arising from the Northern Arm being ionized on one side by radiation from the central star cluster, and 5) the forces accompanying shocks from the collisions of gas streams such as the Northern Arm and the Circumnuclear Disk. The divergence of forces experienced by the stars and gas is likely most pronounced for IRS 21, which is at the apparent leading edge of this train of sources.

An alternative hypothesis to having the Northern Arm sources form within the Northern Arm, while still allowing them to be young, is to admit that they are members of the central parsec cluster of apparently young, luminous emission-line stars, but that they be fortuitously embedded within or superimposed upon the Northern Arm. Based on $\sim 10\%$ coverage of the central parsec by the Northern Arm, however, the chance³ that these are intrinsically mid-infrared sources that are accidentally superimposed on the Northern Arm is less than 10^{-4} .

These considerations lead us to suppose that the Northern Arm sources may be ambient, luminous stars of the Galactic Center population that are presently embedded in the Northern Arm. In order to assess this hypothesis, we have undertaken a study of the photometry and spatially resolved structure of IRS 21 at near- and mid-infrared wavelengths, using diffraction limited imaging with the W.M. Keck 10-m telescopes. At the distance to the Galactic Center, 8 kpc (Reid 1993), the angular resolution of these images at the wavelength extremes of this study ($0''.05$ at $2.2\ \mu\text{m}$ and $0''.31$ at $24.5\ \mu\text{m}$) correspond to 400 AU and 4960 AU, respectively, and are a factor of 2-3 times better than previous measurements (Ott et al. 1999; Gezari 1992).

2. Observations & Data Reduction

³ Within the central parsec, six of the eight strong mid-infrared sources lie along the Northern Arm.

2.1. Near-Infrared Images

Speckle imaging observations of IRS 21 were obtained in the K [$2.2\ \mu\text{m}$] bandpass using the W. M. Keck I 10-meter telescope and the facility near-infrared camera (NIRC; Matthews & Soifer 1994; Matthews et al. 1996) on the nights of 1995 June 10-12, 1996 June 26-27, 1997 May 13, 1998 April 2, 1998 May 14-15, 1998 August 4-6, 1999 May 2-4, and 1999 July 24-25. During these observations, the long-exposure seeing at $2.2\ \mu\text{m}$ averaged $\sim 0''.6$. The majority of the images were obtained for a proper motion study of the central stellar cluster (Ghez et al. 1998, 2000) and were, therefore, centered roughly on the nominal position of Sgr A* ($3''$ Northwest of IRS 21); some images taken in 1998 August were centered on IRS 21. During most observations, additional frames were also obtained to construct a larger mosaic, which included the three stars necessary to tie the near-infrared reference frame to both the radio and mid-infrared reference frames (IRS 7, IRS 10EE, and IRS 3, Menten et al. 1997). Each observation consisted of several sets of ~ 100 short exposure ($t_{\text{int}} = 0.14\ \text{sec}$) frames, which freeze the distortion introduced by turbulence in the Earth’s atmosphere. Each of these speckle frames, which have a pixel scale of $0.0203 \pm 0.0005\ \text{arcsec/pixel}$ and a corresponding field of view of $5'' \times 5''$, contain high spatial resolution information that is recovered in post-processing.

Diffraction-limited images were obtained from the speckle frames using the technique described in detail by Ghez et al. (1998). In brief, the individual frames were processed in the standard manner: bad-pixel-corrected, sky-subtracted, sub-pixelated by a factor of two and flat-fielded. The shift-and-add (SAA) images were generated by combining sets of 100 frames that have been shifted to align the brightest speckle of a bright point source located near the center of the field of view (either IRS 16C or IRS 33E for the frames centered on IRS 21). The resulting SAA point spread function (PSF) consists of a seeing halo and a diffraction limited core ($\theta_{\text{diff}} \simeq 0''.05$) containing $\sim 2\text{-}5\%$ of the total light (see Figure 1).

Additional K-band observations of IRS 21 were obtained with the W.M. Keck II Adaptive Optics (AO) system (Wizinowich et al. 2000) on the night of 1999 May 5. In these observations, USNO 0600-28579500, which has an R ($0.7\ \mu\text{m}$)-band magnitude of 13.2 and is $33''$ away from IRS 21, served as the natural guide star. The 256×256 near-infrared camera, KCAM, used behind the AO system, has a plate scale of $0.0171 \pm 0.0004\ \text{arcsec/pixel}$. The plate scale was established based on the NIRC plate scale using the relative distances between IRS 16C, IRS 16SW, and IRS 16NE, as measured with KCAM and NIRC. The AO images, which consist of five-second exposures, were calibrated and sub-pixelated in the same manner as the speckle frames. Five images, out of total of nine, with the best AO performance (core size less than $0''.2$) were registered and averaged together. The PSF of the final image has a core-halo structure, with a core size of $0''.12$ and 13% of the light

contained within the core. Compared to the AO performance on the Galactic Center earlier in the evening, as reported by Wizinowich et al. (2000), the AO performance during the IRS 21 observation was significantly degraded so that only half as much energy was seen in the core. Nonetheless, compared to the typical PSF in the speckle images, the AO PSF for the IRS 21 observations has ~ 5 times more energy in the core but a core size that is about twice as broad. Neither the speckle nor AO data were flux calibrated.

2.2. Mid-Infrared Images

Mid-infrared images of the central parsec were obtained through narrow-band filters at 8.8, 12.5, 20.8, and 24.5 μm ($\Delta\lambda = 0.87, 1.16, 1.65, 0.76 \mu\text{m}$, respectively) with the MIRLIN mid-infrared camera (Ressler et al. 1994), which has a plate scale of 0.137 ± 0.003 arcsec/pixel, based on the NIRC plate scale and the NIRC and MIRLIN measurements of the relative distances between IRS 7 and IRS 3, and a field of view of $17'' \times 17''$ when mounted on the W. M. Keck II 10-meter telescope. The 8.8 and 24.5 μm data were obtained on 1998 March 13 & 16 while the 12.5 and 20.8 μm data were collected on 1998 June 14-15. Images of the Galactic Center and a set of reference stars (α Sco, α Boo, α Lyr, β Leo and σ Sco) were taken throughout the night, allowing for photometric⁴ and PSF calibration. For these observations, the chopping secondary was operated at a frequency of ~ 4 Hz with an amplitude of $15''$ at a position angle of 315° in March and $30''$ at 135° , 150° , and 170° in June. Likewise, the telescope was nodded at a frequency of 0.04 Hz with an amplitude of $60''$ at a position angle of 270° in March and $90''$ at a position angle of 225° in June. Each chop image had a integration time of 10-70 milliseconds with 4-12 coadds per image and 100-200 chops per frame resulting in a total on-source integration time ranging from 5 to 15 minutes over the wavelength range covered. The chop-nod pairs were double differenced, flat-fielded, bad pixel corrected, airmass calibrated, sub-pixelated by a factor of 6, registered and then rebinned by 2 pixels to create a $\sim 25'' \times 25''$ mosaic of a region centered on Sgr A* and including IRS 21 (see Figure 2). The intrinsic fluxes for the photometric standard stars are estimated using the convolution of the MIRLIN filter transmission and the quantum efficiency curves with the spectra of the photometric standard stars provided by Cohen et. al (1992). Figure 3 shows the color map, centered on IRS 21, constructed using the flux calibrated 12.5 and 20.8 μm images.

⁴At 8.8 μm , there were an insufficient number of reference stars observed to establish an accurate zero point. We, therefore, used the Stolovy et al. (1996) measurements of IRS 7 and IRS 3 to obtain a zero point for our 8.8 μm map.

3. Results

3.1. Near-infrared Size of IRS 21

The remarkable extent of IRS 21 at $2.2\ \mu\text{m}$ is evident in Figure 4, which contrasts the $2.2\ \mu\text{m}$ image of IRS 21 and the point source, IRS 33E (Blum et al. 1996). The image of IRS 21 shows no significant deviation from circular symmetry at this spatial resolution. Therefore, our analysis of its size is performed in one dimension by comparing the azimuthally-averaged intensity profile of IRS 21 with that of the PSF. Due to their relatively isolated positions within the $2.2\ \mu\text{m}$ images, IRS 16NE is used as the PSF for all of the near-infrared central cluster images, while IRS 33E is used as the PSF for those images having IRS 21 centered in the field of view. Both IRS 16NE and IRS 33E appear to be unresolved stars at this resolution. Since the source density in this region is large, a circular area with a radius of $0''.6$ around any neighboring sources brighter than $m_K \sim 14$ is excluded from the azimuthal averages. Each pixel included in the average is weighted by the number of frames that contributed to its value in the SAA processing or AO averaging. The background is subtracted on the basis of the median value of the radial profile between $1''.0$ and $1''.1$. Figure 5 shows examples of the resulting radial profiles for IRS 21 and a PSF.

Once the radial intensity profiles are extracted, an intrinsic size is estimated by modeling the observed IRS 21 profile as the convolution of the PSF profile with a Gaussian function. Figure 5 also shows the best fitting model profile, from which we use the Gaussian HWHM to assign an intrinsic radius of IRS 21 for each image. Table 1 lists the average radius and standard deviation from all epochs of $2.2\ \mu\text{m}$ data. The $2.2\ \mu\text{m}$ radius derived from the SAA images appears to have remained constant from 1995 to 1999, with a weighted average and uncertainty of 725 ± 40 AU for all epochs of data. Although the AO result is somewhat smaller, 570 ± 40 AU, this is most likely due to a mismatch between a Gaussian and the true intrinsic shape. Nonetheless, this modeling allows us to assign an effective size, which we take to be the average of these two values, 650 ± 80 AU, assigning the half-range as our uncertainty.

3.2. Mid-infrared Size, Identification and Fluxes of IRS 21

Figure 6 (column 1) shows the $2.2\ \mu\text{m}$ position of IRS 21 in the 8.8, 12.5, 20.8, $24.5\ \mu\text{m}$ maps of IRS 21, based on the near- and mid-infrared positions of IRS 7 and IRS 3. Within the $2'' \times 2''$ region displayed, IRS 21's mid-infrared emission peaks within $0''.1 \pm 0''.1$ of its $2.2\ \mu\text{m}$ position. A second mid-infrared peak is also detected $0''.5$ Northwest of IRS 21; however, the color map provided in Figure 3 shows that only the source associated with IRS 21 has

a color that is distinguishable from the background. This suggests that the neighboring source is an externally heated region of increased dust density as was first proposed to be the case for IRS 21 (Gezari et al. 1985).

The structure of the diffuse background emission from the Northern Arm and the close proximity of the neighboring source (see Figures 2 and 6) complicates the analysis of the extent of IRS 21 at mid-infrared wavelengths compared to that carried out at $2.2\ \mu\text{m}$. In order to separate IRS 21 from the background emission of the Northern Arm, which has a ridge-like structure, and neighboring source, we apply an algorithm similar to CLEAN (Hogbom 1974), which removes IRS 21 from the image, leaving only the diffuse emission. Since IRS 21 lies on the edge of the Northern Arm, we create a first-order approximation of the surrounding background emission by fitting an inclined plane to the region within an annulus, $1''.0$ in outer radius and $0''.2$ wide, around the position of IRS 21. To avoid the flux from the discrete neighboring source when fitting the plane, the area within $0''.4$ of the source ($\sim 25\%$ of the annulus) was excluded from the fit. After subtracting the inclined plane from the image, the CLEAN algorithm iteratively subtracts a scaled ($\gamma=0.5$) PSF from the position of the peak flux within a $1''.0$ cleaning radius of the position of IRS 21. Here, where a 2-D estimate of the PSF is necessary, the independently observed photometric standards were used as estimates of the PSF. The progress of the cleaning algorithm is monitored by calculating the average flux within the cleaning radius and is halted when this flux falls below zero. Two maps are created by this procedure, a residual map and a delta map (see Figure 6). The residual map (not shown) contains only the background emission from the Northern Arm and the delta map contains IRS 21 and a small contaminating contribution from the neighboring source. In order to isolate IRS 21, those clean components within a radius of $0''.4$ from the position of the neighboring source as well as those found within a radial interval of $0''.2$ about the $1''.0$ cleaning radius are reconvolved with the scaled PSF and added back into the residual map. Since the resulting residual map should represent the diffuse emission of the Northern Arm and the neighboring source, subtracting it from the original image leaves only the flux from IRS 21 (depicted in column 2 of Figure 6).

The radial extent of IRS 21 at mid-infrared wavelengths is estimated from azimuthally-averaged radial intensity profiles of the background-subtracted images with the same method used to analyze the $2.2\ \mu\text{m}$ profiles, with one additional step. An estimate of the systematic uncertainty from the imposed size of the cleaning radius is obtained by varying the cleaning radius from $0''.9$ to $1''.1$. This is added to the statistical uncertainty, which is estimated using the RMS of the results from the analysis on the three sub-sets of the MIRLIN images. The statistical uncertainties are the dominant source of error (§ 3.1). The radial extent of IRS 21 is estimated at each wavelength (see Figure 7) using the following two sources for the PSF: (1) the photometric standard star and (2) IRS 7,

which is in the same field of view as IRS 21 but for which IRS 3 was masked out in order to create an accurate 1-D PSF estimate. At all wavelengths except $8.8\ \mu\text{m}$, the separately observed PSF star and IRS 7 have a FWHM that corresponds roughly to the diffraction limit and therefore yield comparable results. The values quoted in Table 2 at these longer wavelengths are based on the separately observed PSF. Between 12.4 and $24.5\ \mu\text{m}$ the size estimates are not significantly different as a function of wavelength and produce a mean radius for IRS 21 of 1600 ± 200 AU. At $8.8\ \mu\text{m}$, the FWHM of IRS 7 and IRS 3 are both twice as large as that of the separately observed point source, β Leo (see Table 2), suggesting a change in atmospheric conditions (i.e., the IRS 21 images at $8.8\ \mu\text{m}$ are seeing limited). Since the radial profile of the simultaneously observed IRS 7 is comparable in size to IRS 21 at $8.8\ \mu\text{m}$, we cannot estimate a size for IRS 21 at this wavelength and do not include this radial profile in our modeling presented in §4. A 3σ upper limit to the $8.8\ \mu\text{m}$ size of IRS 21 (<1830 AU) is assigned. This is based on the FWHM of the Gaussian which, when convolved with the radial profile of IRS 7, results in a reduced chi squared value of 3 between the model and observed radial profile.

Table 2 also lists the mid-infrared fluxes measured for IRS 21 by comparing the total counts within a $1''.0$ radius circular aperture in the IRS 21 image with and without the background subtracted (column 2 in Figure 6) to the counts within the same aperture around a photometric standard star. We estimate that IRS 21 is 31, 15, 6 and 6% above the background value in the original images at 8.8 , 12.5 , 20.8 and $24.5\ \mu\text{m}$, respectively. The uncertainties for the fluxes given in Table 2 are the sum of the systematic and statistical uncertainties as estimated by the same method used for the mid-infrared sizes. Compared to the previously reported $8.7\ \mu\text{m}$ flux value of 5.6 ± 2.0 Jy by Stolovy et al. (1996) using a $2''$ circular aperture and no background removed, our values are lower due to a smaller aperture size. Using the same $2''$ circular aperture and not removing the Northern Arm contribution, we obtain a comparable value of 3.6 ± 0.1 Jy at $8.8\ \mu\text{m}$. No other mid-infrared photometry for IRS 21 has been reported in the literature.

4. Discussion

4.1. Origin of the Near- and Mid-infrared Dust Cloud

The immense size of IRS 21 at $2.2\ \mu\text{m}$ (~ 650 AU) and in the mid-infrared (~ 1600 AU) is well beyond that expected for a stellar photosphere by over two orders of magnitude. For comparison, the radius of the largest stellar photosphere, an M super-giant, is roughly 4 AU (Drilling & Landolt 2000). We are, therefore, most likely detecting an extended distribution of dust around IRS 21. The color temperature of IRS 21 from our MIRLIN data (see

Figure 3) shows that it is hotter than the surrounding Northern Arm dust, suggesting that it is self-luminous and, therefore, has a central radiative source (Gezari 1992). If the dust is intrinsic to the heating source, it could be in the form of an inflow, as in the case of a protostar, or an outflow of material, as in the case of, for example, a Wolf-Rayet star, a luminous blue variable (LBV), or an M supergiant. Alternatively, the dust could be associated with the infalling Northern Arm, either passively heated by a central radiative source and/or dynamically perturbed by the stellar winds of IRS 21. In either case, the Roche limit for a star of mass, M , at the projected distance of IRS 21 from Sgr A* is $480 \text{ AU} (M/10 M_{\odot})^{1/3}$, which suggests that the current dust distribution is transitory rather than being a long-lived configuration or a static shell. This implies that the dust is unlikely to be part of an inflow (unless the projection effects are quite strong), adding to the list of difficulties for the young stellar object hypothesis introduced in §1.

4.2. The Spectral Energy Distribution

Construction of the spectral energy distribution (SED) for IRS 21 provides additional insight into the nature of the source. Figure 8 combines our mid-infrared flux densities for IRS 21 and the Northern Arm (see Table 2) along with others collected from the literature (references given in the Figure 8 caption). All of the photometry from the literature is calibrated using zero points from Cohen et al. (1992) and dereddened assuming a visual extinction of $A_V=30$ and an ISM extinction law based on observations of extinction at the Galactic Center (see Moneti et al. 2001 and references within). The shape of the dereddened SED suggests there are two distinct components: one in the near-infrared responsible for the flux between $2\text{--}4 \mu\text{m}$, and a separate, mid-infrared component. The mid-infrared component is assumed to be thermal emission from dust heated by both the central source and through the trapping of external Lyman α photons. The latter is necessary to achieve the grain temperatures required to model the mid-infrared component of the SED (see Rieke, Rieke, & Paul 1989 and references within). We ascribe the near-infrared component to dust scattering as well as extincted light from the central source. Scattering is further supported by the large $2.2 \mu\text{m}$ polarization (Ott et al. 1999). This implies an asymmetry in the dust distribution that is below our angular resolution.

To utilize both the spectral and spatial information, we have created a simple 2-D radiative transfer code that simultaneously fits the 2.2 to $24.5 \mu\text{m}$ flux densities and the radial profiles including both the flux from IRS 21 and the Northern Arm (see Figure 8). The basis for the model is a central blackbody embedded in a distribution of gas and dust, which singly scatters or absorbs light from the central source. The central radiative source

is described by two free parameters: its radius, R_{cen} , and temperature, T_{cen} . In addition to the internal heating from the central blackbody, an external heating contribution is added in the form of Lyman α trapping⁵. For simplicity, we assume that the same, single population of dust grains is responsible for both the thermal and scattering component. This model does not account for grain heating due to light scattered within the dust. Fixed in this model are (1) the gas to dust mass ratio of 100:1 (2) the dust’s emission and scattering coefficients, which are assumed to be those derived for silicate grains⁶ by Laor & Draine (1993) and (3) the distribution of dust grain radii, $n(a)$, which is assumed to depend on dust size, a , as $n(a) \propto a^{-3.5} da$ from 0.02 to 0.25 μm (Mathis et al. 1977, MRN). A number of possible dust density profiles are considered, including a constant dust density model, which represents passive heating of the Northern Arm (§4.3), a $1/r^2$ dust density model appropriate for an outflow or inflow of material assuming a constant velocity (§4.4), and a “bow shock” dust density model, which would be expected if the Northern Arm were interacting with stellar winds from the central radiative source (§4.5).

Model fitting proceeds by minimizing the reduced χ^2 value for both the SED and four (2.2, 12.5, 20.8 and 24.5 μm) radial profiles⁷ simultaneously. We’ve chosen to equally weight the near-infrared photometry, mid-infrared photometry, the near-infrared profile, and the mid-infrared profiles ($\tilde{\chi}_{tot}^2 = \frac{1}{2}\tilde{\chi}_{SED}^2 + \frac{1}{4}\tilde{\chi}_{2.2profile}^2 + \frac{1}{12}\tilde{\chi}_{12.5profile}^2 + \frac{1}{12}\tilde{\chi}_{20.8profile}^2 + \frac{1}{12}\tilde{\chi}_{24.5profile}^2$). The weighted reduced chi squared provided above is minimized to find the best fitting value for each free parameter. In order to avoid local minima, this is done using 100 iterations of the Powell minimization algorithm with randomly chosen sets of initial parameters (Press et al. 1992). The range of the initial values is set to cover a reasonable portion of acceptable values for the physical parameters. The uncertainty in each fitted parameter is estimated using the amount of variation around the best-fit value that produces a deviation in χ_{tot}^2 representing a 3σ confidence level given the number of free parameters in each model (Press et al. 1992).

⁵Lyman α trapping is a function of the gas density, n_H , which is estimated through the dust density and the gas to dust mass ratio. It is also a function of $z_{L\alpha}$ which is the fraction of recombinations resulting in the production of a Ly α photon. This parameter is dependent on the electron temperature, which is assumed to be 7,000 K (see Roberts & Goss 1993) resulting in a recombination fraction of 0.7 (Spitzer 1978)

⁶The mid- to far-infrared spectrum of the Northern Arm has been previously modeled with optically thin silicate emission by Chan et al. (1997). Furthermore, graphite grains produce significantly worse fits for the SED models.

⁷The near- and mid-infrared radial profiles are rebinned to match the original plate scales prior to convolution with the radial profile of the PSF.

4.3. Constant Dust Distribution

As a first guess to the distribution of the dust around IRS 21, we place the central heating source within a constant density of material. The only free parameters for the constant dust density model are the size and temperature of the central source, the radius of the inner edge of the dust, r_i , and the dust mass density, ρ_d . Table 3 gives the parameters of the best fitting model ($\tilde{\chi}^2=800$). This model did not provide an acceptable fit to the radial profiles as it produces too much flux in the wings of the mid-infrared profiles (Figure 8, top row). This suggests that the dust density falls off at some distance from the inner edge of the dust envelope as might occur if the surrounding dust were undergoing some type of dynamical process, either intrinsic mass in- or out-flow or interaction with the Northern Arm. Based on this analysis, we rule out the model in which the infrared extended emission arises from dust in the Northern Arm that is passively interacting with an embedded central source.

4.4. $1/r^2$ Dust Distribution

For a constant mass flow rate, a spherical outflow or inflow will produce a $1/r^2$ density distribution. The free parameters for the dust distribution in this model include the radius of the inner and outer edge of the dust, r_i and r_o , the dust mass density at the inner edge, ρ_d , and the dust density of the surrounding Northern Arm, ρ_{NA} . This results in a total of six free parameters, including the temperature and radius of the central source. Table 3 gives the parameters and errors for the best fitting model ($\tilde{\chi}^2=80$) which is also plotted in Figure 8 (middle row). The size and temperature of the central source are suggestive of an embedded, optically thick dust shell. The inner and outer extent of the dust are consistent with the near- and mid-infrared Gaussian sizes listed in Tables 1 and 2. The luminosity of the central object ($10^4 L_\odot$) allows for several possibilities for its identity: a massive main sequence or post-main sequence early-type star ($M > 25 M_\odot$), a massive AGB star, or a Wolf-Rayet star (see Table 4).

Although the $1/r^2$ model yields a somewhat reasonable fit to the SED and radial profiles, given the simplicity of the model, there are arguments against the constant mass flow model. Using the derived gas density and typical outflow velocities of luminous stars in Table 4, we estimate mass-loss rates (column 5) which are at least an order of magnitude above the values expected for all of the stellar candidates. Furthermore, no known intrinsic outflow source has an observed infrared radius due to optically thin emission comparable to that observed for IRS 21 (~ 650 AU at $2.2 \mu\text{m}$ and ~ 1640 AU at mid-infrared wavelengths). Examples of large resolved outflow sources at $2.2 \mu\text{m}$ include the spiral dust shell around

the binary Wolf-Rayet star, WR 104, and the dust shell around the Wolf-Rayet star, Ve 2-45, which have diameters of 160 AU and 70 AU, respectively (Tuthill, Monnier, & Danchi 1999; Danks et al. 1983). The well-studied carbon star IRC +10216, whose dust shell is optically thick at $2.2 \mu\text{m}$, has an estimated radius of ~ 50 AU (Rowan-Robinson & Harris 1983). There are protostellar objects with $2.2 \mu\text{m}$ radii on the order of a few hundred AU as measured using speckle interferometry (Howell, McCarthy & Low 1981), but as discussed in §1 and §4.1 there are difficulties with the protostellar hypothesis. These arguments suggest that the constant mass flow model alone is not a suitable model for IRS 21.

4.5. Bow Shock Dust Distribution

A model that allows for a condensed dust distribution without requiring a large intrinsic dust outflow, is a “bow shock” model. The bow shock dust density profile is modeled as a spherical shell, with a constant dust density from an inner radius of r_i to an outer radius of r_o . While a bow shock does not wrap completely around the star which produces it, we judge that the spherical approximation will provide a reasonable estimation of the radial profiles and the photometry in the case of a relatively face-on bow shock. Table 3 gives the parameters and errors for the best fitting model ($\tilde{\chi}^2=30$), which is shown in the bottom row of Figure 8. The gas density of the Northern Arm is consistent with the expected value of 10^5 cm^{-3} given by Genzel et al. (1998). We argue below that the bow shock model is a physically sensible explanation for the optically resolved structure⁸.

The temperature and radius of the *central source* as well as the lack of any observed photospheric lines suggest that it is an optically thick dust shell from a $1.3 \times 10^4 L_\odot$ mass losing star. This central source is surrounded by the optically thin dust that has been modeled here as a bow shock to explain the resolved emission. However, the luminous sources listed in Table 4 are not equally capable of producing bow shocks from interactions with the Northern Arm at a distance of ~ 1000 AU. We have estimated the stand-off distance, l , which is defined as the distance at which the ram pressure from the intrinsic stellar wind equals that of the motion of the material flowing along the Northern Arm. $l = 1.74 \times 10^{19} \dot{m}_*^{1/2} v_w^{1/2} v_*^{-1} \mu_H^{1/2} n_H^{-1/2} \text{ cm}$, where \dot{m}_* is the stellar mass loss rate in units of 10^{-6}

⁸Since this simple radiative transfer model contains a number of assumed, but undetermined parameters, we do not report formal uncertainties. A better fit to the $2.2 \mu\text{m}$ radial profile can be achieved using a larger upper limit to the grain size. The addition of larger grains to the grain population increases the scattering coefficient such that the $2.2 \mu\text{m}$ flux contains a greater fraction of scattered light. This results in a $2.2 \mu\text{m}$ radial profile with a broader core, thus providing a better fit to the observed near-infrared radial profile. We, however, do not feel that this is evidence for large grains, given the simplicity of the model.

$M_{\odot} \text{ yr}^{-1}$, v_w is the stellar wind velocity in units of 10^8 cm s^{-1} , v_* is the motion of the star through the Northern Arm in units of 10^6 cm s^{-1} , μ_H is the mean molecular weight and, n_H is the gas density of the Northern Arm in units of cm s^{-1} (Weaver et al. 1977). We assume a relative velocity of $\sim 100 \text{ km s}^{-1}$ between IRS 21 and the Northern Arm material (Herbst, Beckwith, & Shure 1993), the dust density of the Northern Arm derived from the bow shock radiative transfer model, ρ_{NA} , and the mass loss rates and stellar wind velocities of each candidate as found in the literature (see Table 4). The resulting bow shock distances are given in column 6 of Table 4. While there are many stars with luminosities near that of IRS 21, they have a range of stellar wind velocities and mass loss rates affecting their expected stand-off distance. Based on comparison of the derived stand-off distances and the observed size of IRS 21, we dismiss the possibility that IRS 21’s central source is a giant star, like IRS 7, and suggest that it is possibly a massive star in a more evolved state, such as a Wolf-Rayet or AGB star.

The bow shock scenario is appealing because it explains the association of IRS 21 and the Northern Arm without requiring that the central source be formed within the Northern Arm before or during the infall toward Sgr A*. A bow shock instead requires the much more plausible circumstance that IRS 21 is simply passing through the Northern Arm, resulting in an interaction with its intrinsic stellar winds. The apparent absence of the characteristic horse-shoe geometry indicative of a bow shock, can be attributed to the orientation (if the vector representing the relative velocity of IRS 21 and the Northern Arm is oriented predominantly toward or away us) or to the depth at which the central heating source is embedded within the Northern Arm. Scattered light by an asymmetric dust distribution, however, would explain the large observed K-band polarization (Ott et al. 1999). Finally, the bow shock model receives support from the recent $2.2 \mu\text{m}$ Gemini AO observations of a clear bow shock structure surrounding the possibly analogous Northern Arm source, IRS 8, located $32''$ north of IRS 21 (Rigaut 2001).

5. Summary and Conclusions

The near- and mid-infrared light from IRS 21, a luminous source at the Galactic Center, has been spatially resolved, giving a remarkably large radius of $\sim 1000 \text{ AU}$. Using this size information along with the $1\text{--}25 \mu\text{m}$ photometry, we suggest that IRS 21 is embedded in the dense “Northern Arm” component of Sgr A West, and that the obscured starlight is diffusing out through the optically thin dust along this feature. The near-infrared light is scattered and extincted light, which probably originated in a dust photosphere overlying the central star, and the mid-infrared light is thermally re-radiated dust emission from

the optically thin shell. Furthermore, our SED and radial profile modeling, along with high-resolution imaging of the similar Northern Arm mid-infrared source, IRS 8, suggest that the dust surrounding IRS 21 is in the form of a bow shock produced as the Northern Arm encounters the winds from the central star. The bow shock scenario removes the necessity that IRS 21 be a young source that formed within the Northern Arm during or prior to its infall toward Sgr A*, and suggests that the central stellar source emits strong winds, accounting for the observed size. The featureless 2.2 μm spectrum suggests that the central source is an optically thick dust shell surrounding a mass-losing source such as a dusty WC9 Wolf-Rayet star. IRS 21 may serve as a prototype for the other luminous sources lying along the Northern Arm, including IRS 1W, 2, 10W, and 5. Considering the large population of windy He I stars within the central parsec (Sellgren et al. 1990, Genzel et al. 1996), it is plausible that these Northern Arm sources are also producing bowshocks like IRS 21 and IRS 8.

We would like to thank Tetsuya Nagata and Mike Jura for their helpful suggestions on the manuscript and Dan Gezari for providing us with unpublished mid-infrared photometry, we used these fluxes for initial SED fitting prior to the completion of our own mid-infrared analysis. The speckle imaging and mid-infrared work were supported through NSF grants No. AST-9457458 and AST-9988397 and the adaptive optics analysis was funded by the NSF Science and Technology Center for Adaptive Optics, managed by the University of California at Santa Cruz under cooperative agreement No. AST-9876783. Portions of this work were carried out at the Jet Propulsion Laboratory, California Institute of Technology, under and agreement with NASA. Development and operation of MIRLIN is supported by the JPL Director’s Discretionary Fund and by NASA’s Office of Space Science.

REFERENCES

- Aitken, D. K., Smith, C. H., Moore, T. J. T., Roche, P. F. 1998, MNRAS, 299, 743
 Becklin, E. E., Matthews, K., Neugebauer, G., & Willner, S. P. 1978, ApJ, 219, 121
 Blum, R. D., Sellgren, K., & DePoy, D. L. 1996, ApJ, 470, 864
 Chan, K-W, et al. 1997, ApJ, 483, 798
 Cohen, M., Walker, R., Barlow, M. J., Deacon, J. R. 1992, AJ, 104, 1650
 Danks, A. C., Dennefeld, M., Wamsteker, W., & Shaver, P. A. 1983, A&A, 118, 301
 DePoy, D. L., & Sharp, N. A. 1991, AJ, 101, 1324

- Drilling, J.S., & Landolt, A., U., 2000, in Allen's Astrophysical Quantities, 4th edition, ed. A. Cox, AIP Press, 381
- Eckart, A., Genzel, R., Hofmann, R., Sams, B.J., and Tacconi-Garman, L., E., 1995, ApJ, 445, L23
- Figer, D.F., McLean, I.S., & Morris, M. 1999, ApJ, 514, 202
- Genzel, R., Pichon, C., Eckart, A., Gerhard, O. E., & Ott, T. 2000, MNRAS, 317, 348
- Genzel, R., Thatte, N., Krabbe, A., Kroker, H., & Tacconi-Garman, L. E. 1996, ApJ, 472, 153
- Gezari, D., 1992, in The Center, Bulge and Disk of the Milky Way, ed. L. Blitz, Kluwer Academic Publishing Co., Dordrecht
- Gezari, D. et al. 1985, ApJ, 299, 1007
- Ghez, A., Morris, M., & Becklin, E. E., Tanner, A., Kremenek, T. 2000, Nature, 407, 349
- Ghez, A., Klein, B. L., Morris, M., & Becklin, E. E. 1998, ApJ, 509, 678
- Herbst, T., Beckwith, S., Shure, M. 1993, ApJ, 411, 21
- Hogbom, J., A. 1974, A&AS, 15, 41
- Howell, R. R., McCarthy, D. W., & Low, F. J. 1981, ApJ, 251, L21
- Krabbe et al. 1995, ApJ, 447, L95
- Kudritzki, R. & Puls, J. 2000, ARA&A, 38, 613
- Lacy, J. H., Townes, C. H., Geballe, T. R., & Hollenbach, D. J. 1980, ApJ, 241, 132
- Lamers, H. J. G. L. M. & Cassinelli, J. P. 1999, Introduction to stellar winds; New York : Cambridge University Press
- Lang, K., R., 1997, *Astrophysical Data: Planets and Stars*, [New York: Springer-Verlag]
- Laor, A. & Draine, B. T. 1993, ApJ, 402, 441
- Lo, K. Y., Claussen, M., J. 1983, Nature, 306, 647
- Mathis, J., S., Rumpl, W., & Nordsieck, K.H. 1977, ApJ, 217, 425
- Matthews, K., Ghez, A. M., Weinberger, A. J., & Neugebauer, G. 1996, PASP, 108, 615
- Matthews, K. & Soifer, B. T. 1994, in Astronomy with Infrared Arrays: The Next Generation, ed. I McLean, Kluwer Academic Publications (Astrophysics and Space Science, v. 190), 239
- Menten, K. M., Reid, M. J., Eckart, A., & Genzel, R. 1997, ApJ, 475, L111

- Moneti, A., Stolovy, S., Blommaert, J., A., D., L., Figer, D. F., Najarro, F. 2001, *A&A*, 366, 106
- Ott, T., Eckart, A., & Genzel, R. 1999, *ApJ*, 523, 248
- Pasquali, A., Langer, N., Schmutz, W., Leitherer, C., Nota, A., Hubeny, I., & Moffat, A. F. J. 1997, *ApJ*, 478, 340
- Paumard, T., Maillard, J. P., Morris, M., & Rigaut, F. 2001, *A&A*, 366, 466
- Press, W. H., Teukolsky, S., A., Vetterling, W., T., Flannery, B., P. 1992, *Numerical Recipes in Fortran*, (2nd ed., Cambridge University Press)
- Rigaut, F., <http://www.gemini.edu/galactic.html>
- Reike, G., Rieke, M., & Paul, A. E. 1989, *ApJ*, 336, 752
- Reid, M. 1993, *ARA&A*, 31, 345
- Ressler, M., E., Werner, M., W., Van Cleve, J., & Choa, H. 1994, *Exp. Astron.*, 3, 277
- Roberts, D. A., & Goss, W. M. 1993, *ApJS*, 86, 133
- Rowan-Robinson, M., & Harris, S. 1983, *MNRAS*, 202, 797
- Sellgren, K., McGinn, M. T., Becklin, E. E., & Hall, D. N. 1990, *ApJ*, 359, 112
- Simon, M., et al. 1990, *ApJ*, 360, 95
- Simons, D., and Becklin, E. 1996 *AJ*, 111, 1908
- Spitzer, L. 1978, New York Wiley-Interscience, 1978. 333 p.
- Stolovy, S., Hayward, T. L., Herter, T. 1996 *ApJ*, 470, L45
- Tollestrup, E. V., Capps, R. W., & Becklin, E. E. 1989, *AJ*, 98, 204
- Tuthill, P. G., Monnier, J. D., & Danchi, W. C. 1999, *Nature*, 398, 487
- Weaver, R., McCray, R., Castor, J., Shapiro, P., & Moore, R. 1977, *ApJ*, 218, 377
- Wizinowich, P. et al. 2000, *PASP*, 112, 315
- Zinnecker, H., Stanke, T., Kaufl, H. 1996, *The Messenger*, 84, 18

Fig. 1.— A $\sim 3'' \times 3''$ section of a typical $2.2 \mu\text{m}$ SAA image containing IRS 21 ($t_{\text{int}}=26$ seconds). This sub-image, which is composed of data taken on 1999 May 15, shows the contrast between the point source, IRS 33E, and the resolved structure of IRS 21. North is up and east is to the left.

Fig. 2.— Mosaic of a $\sim 25'' \times 25''$ region of the Galactic Center at $12.5 \mu\text{m}$. The Northern Arm sources (IRS 21, 1, 2, 10, and 5), IRS 3, and the red supergiant, IRS 7 are identified. North is up and east is to the left.

Fig. 3.— A $12.5\text{-}20.8 \mu\text{m}$ color map grey scale image of the $1'' \times 1''$ region around IRS 21 along with contours of the same region at $12.5 \mu\text{m}$. The hottest region (dark) in the linear grey scale image is ~ 250 K while the coolest regions (light) are ~ 200 K. The contours plotted represent 90-10% of the peak flux value in 10% increments. The source $0''.5$ Northwest of IRS 21, discussed in §3.2, is absent from the color map suggesting it is an externally heated region of higher dust density as was originally suggested for IRS 21 by Gezari (1985). The cross represents the $2.2 \mu\text{m}$ position and uncertainty of IRS 21. Before the two images were divided, the $12.5 \mu\text{m}$ image was convolved with a $0''.4$ FWHM Gaussian beam to match the angular resolution of the two images. North is up and east is to the left.

Fig. 4.— Contours plots of IRS 21 (left) and its neighboring point source, IRS 33E (right). The contours plotted for IRS 21 and IRS 33E represent 90-50% of the peak value in 10% increments and clearly show that IRS 21 is significantly resolved.

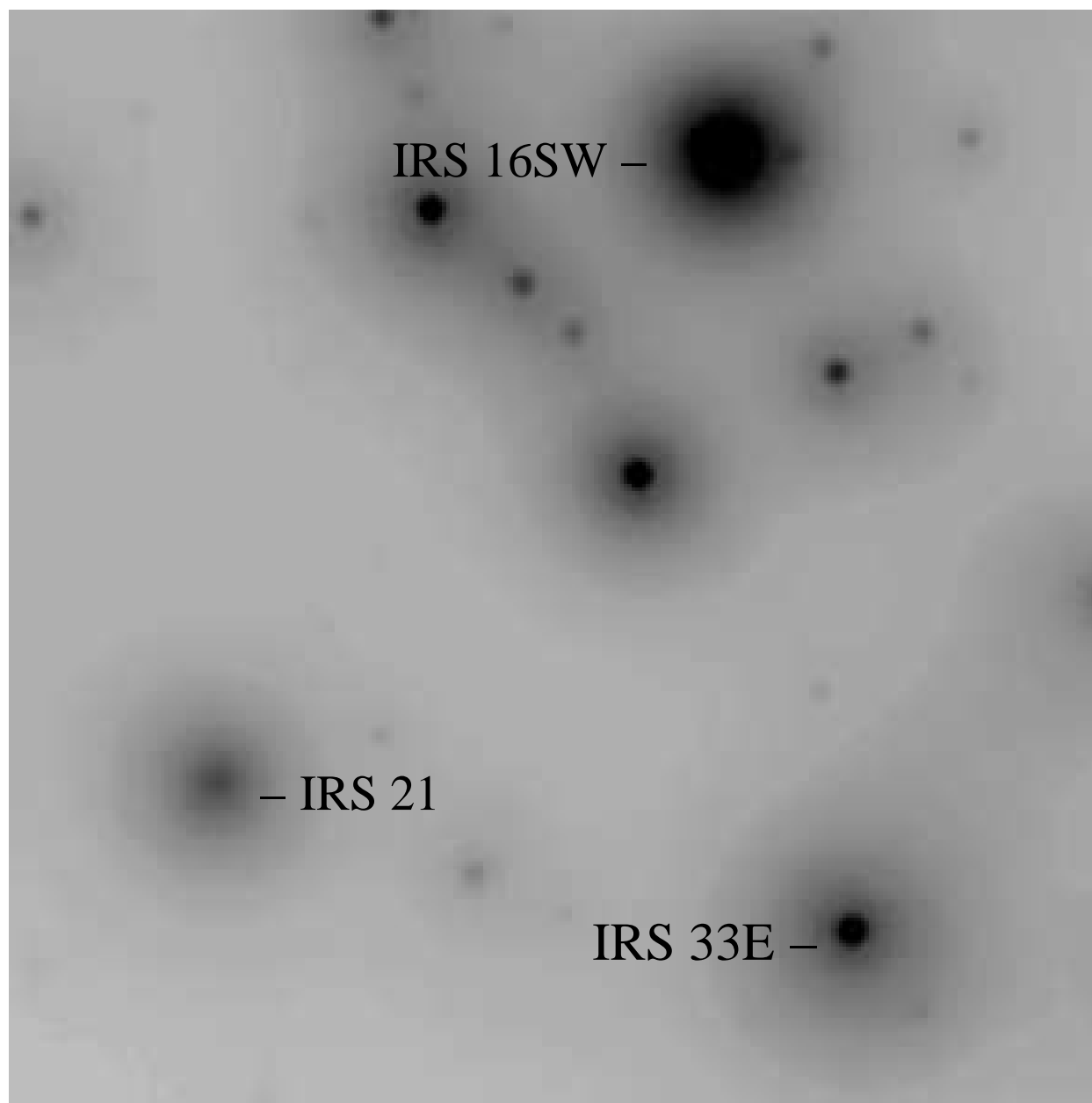
Fig. 5.— Keck AO (left) and SAA (right) radial profiles of IRS 21 (filled circles) and a PSF star (empty circles) along with the profile of the convolution of the PSF with a Gaussian (solid line). This modeling suggests a $2.2 \mu\text{m}$ intrinsic radius of ~ 650 AU. The error bars represent the standard deviation of the mean intensity at each radius.

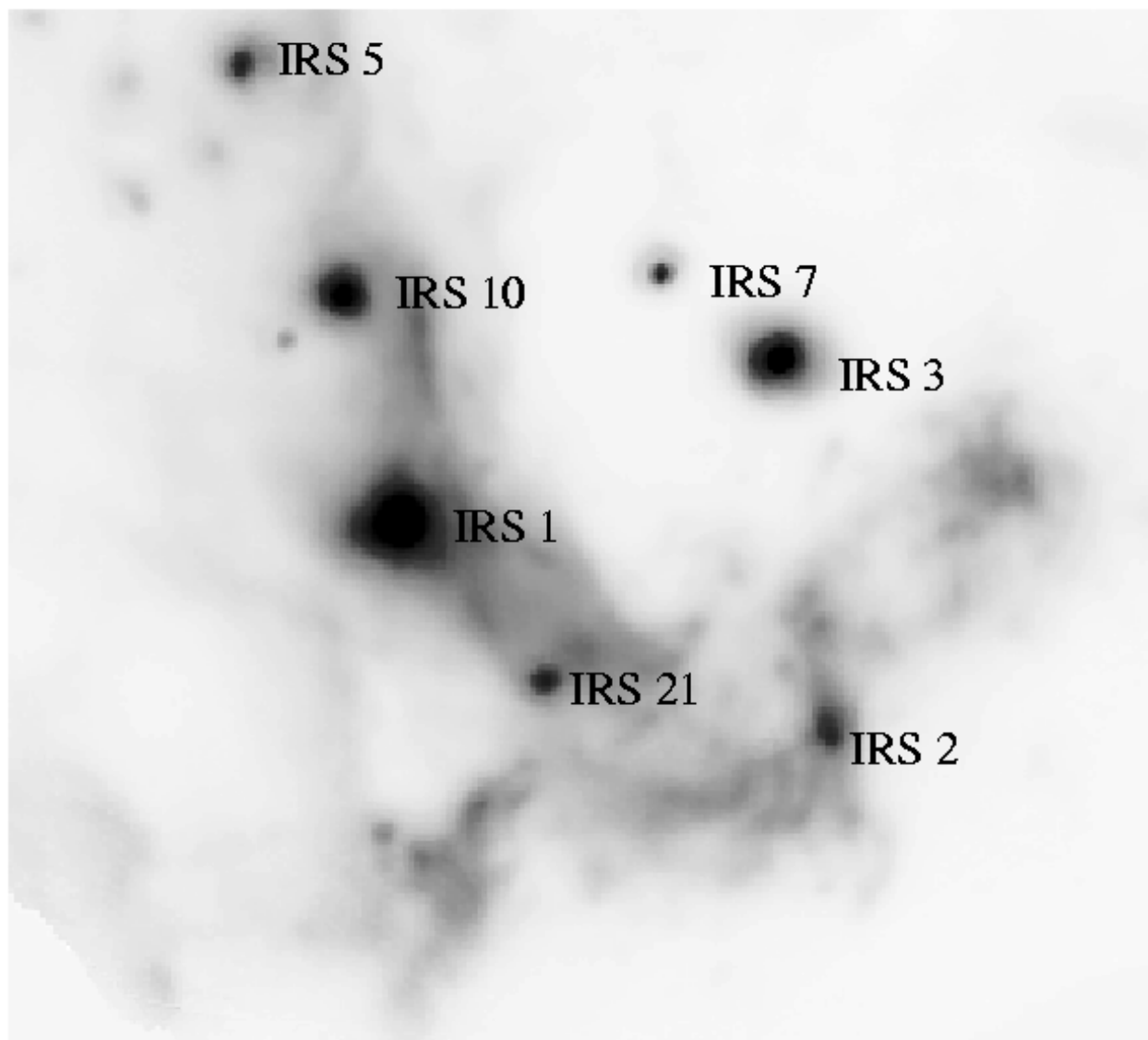
Fig. 6.— Plots of a $3'' \times 3''$ region around IRS 21 showing various aspects of the “cleaning” process (see § 3.2). The original map or “dirty map” and the PSF or “dirty beam” are shown in columns 1 and 3. Column 4 is the delta map depicting the positions and the intensity of the peaks subtracted during the cleaning process including the circles which mark the region around the neighboring source and the annulus around IRS 21 within which the associated flux was added to the background image. Column 2 displays the final image of IRS 21 with the background removed. The contours plotted represent 90-10% of the peak value in 10% increments. The cross represents the position and uncertainty of IRS 21 in the $2.2 \mu\text{m}$ image.

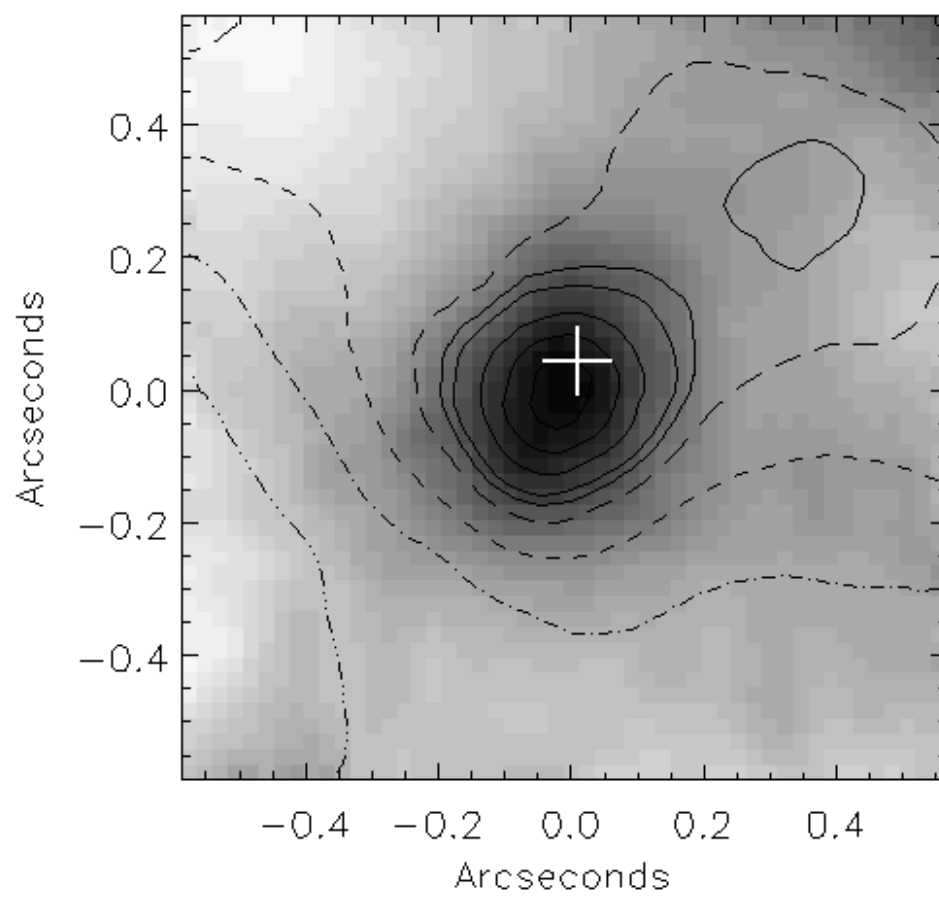
Fig. 7.— a) Radial profiles of the background subtracted images of IRS 21 (filled circles) and a PSF star or IRS 7 ($8.8 \mu\text{m}$ only) (empty circles) along with the profile of the convolution

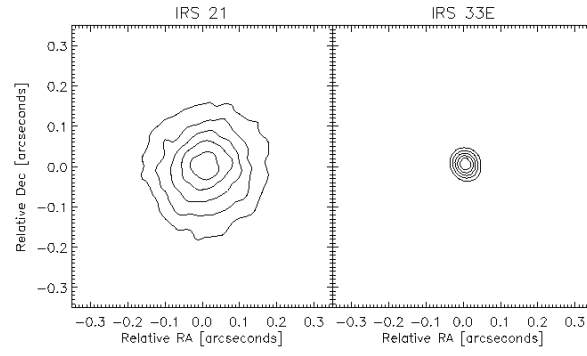
of the PSF with a Gaussian (solid line) at 12.5, 20.8 and 24.5 μm . This model suggests a mid-infrared radius of ~ 1640 AU.

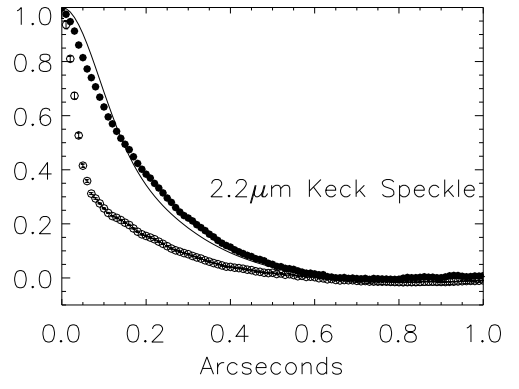
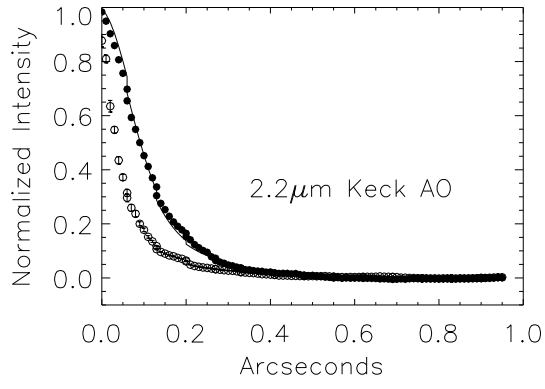
Fig. 8.— *Left column* - De-reddened photometry and the best fitting constant (top), $1/r^2$ (middle), and bow-shock (bottom) radiative transfer models for IRS 21 showing the two components of the SED - the near-infrared scattered light (dot-dashed line) and mid-infrared re-emitted light (dashed line) - as well as the sum of the two components (solid line). References - J (1.25 μm) - Blum et al. 1996; (1.45 μm) - Stolovy private com.; H (1.6 μm) - Blum et al. 1996; (1.9 μm) - Stolovy private com.; K (2.2 μm) - Blum et al. 1996, DePoy & Sharp 1991, Simon et al. 1990 ; L (3.5 μm) - Tollestrup, Capps & Becklin 1989 ; L' (3.8 μm) - Simons & Becklin 1996 ; 8.8-24.5 μm - this work. *Right column* - Radial profiles of IRS 21 (filled circles) along with the profile of the convolution of the PSF with the radial profile created by the constant (top), $1/r^2$ (middle), and bow-shock (bottom) radiative transfer models at 2.2, 12.5, 20.8 and 24.5 μm (solid line). The mid-infrared photometry and radial profiles include a constant background term, which is modeled to arise from Lyman α trapping in all cases.

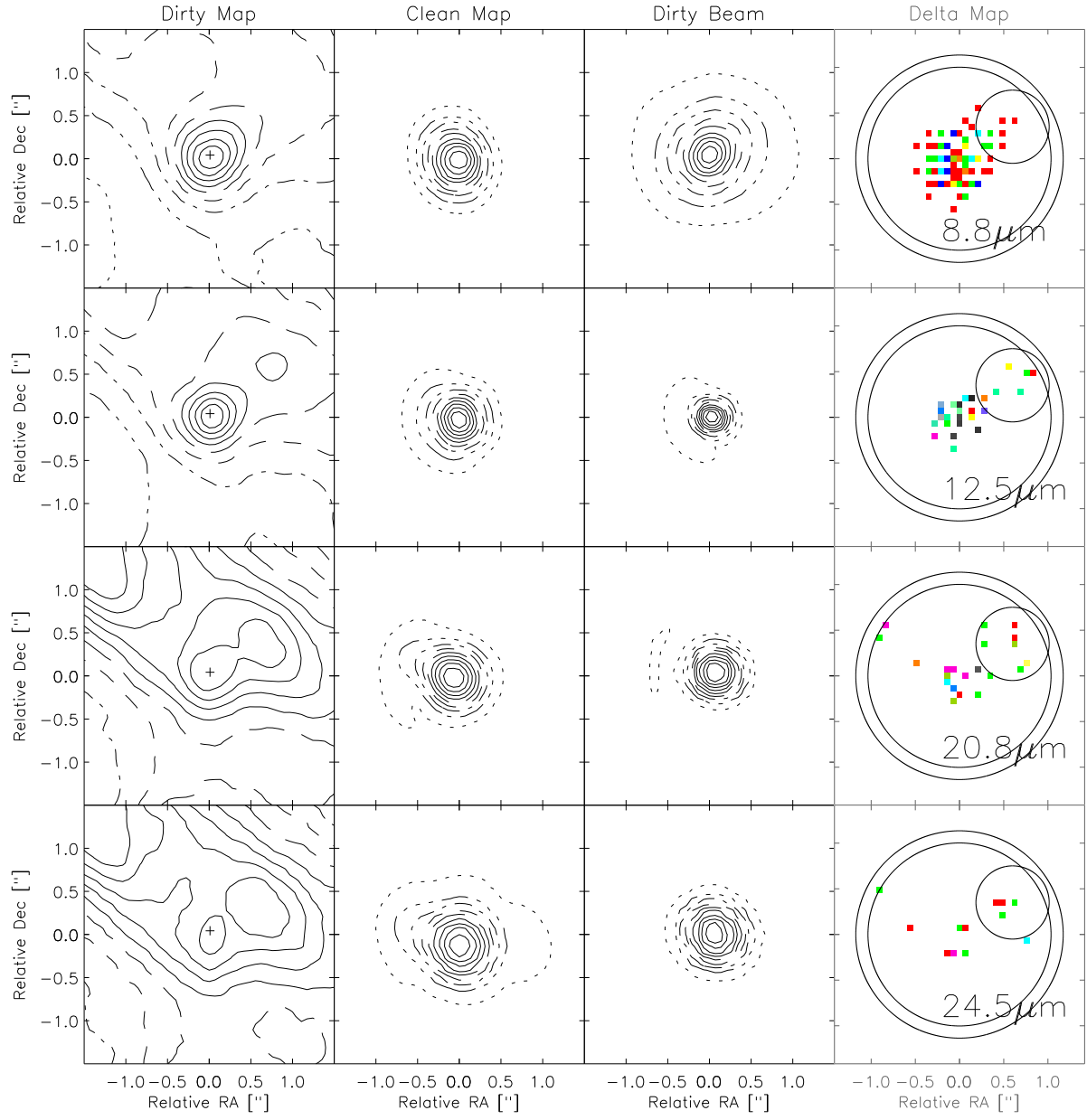


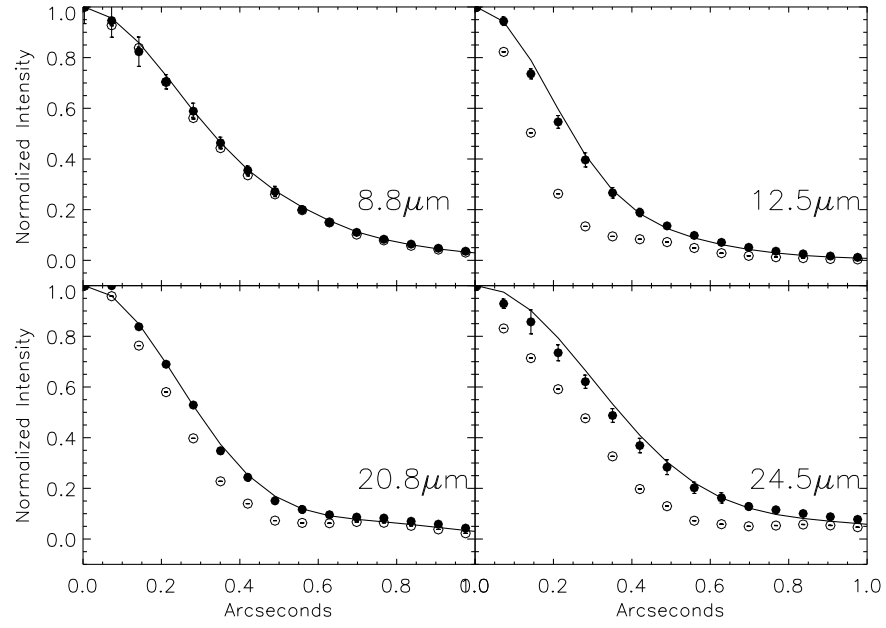












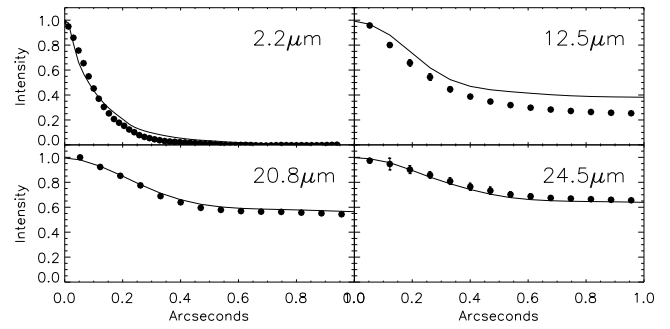
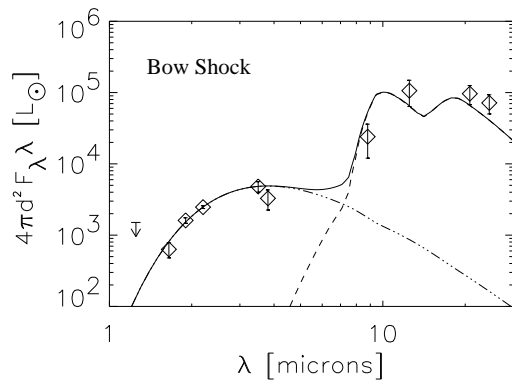
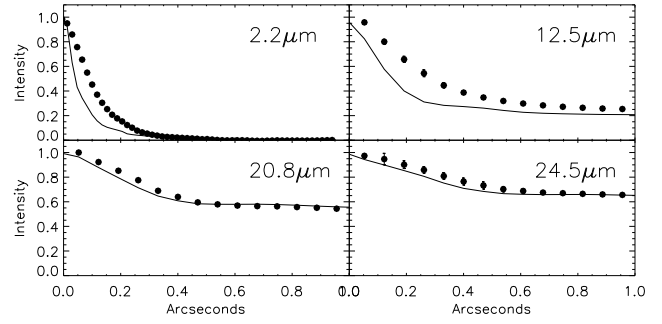
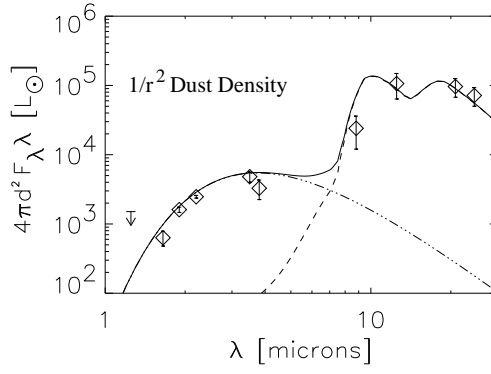
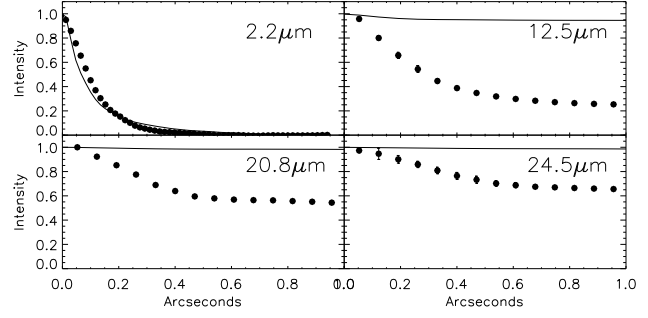
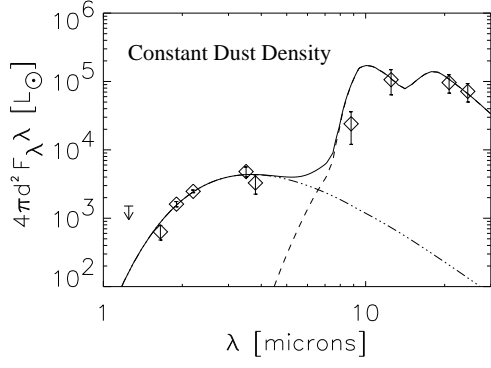


Table 1. 2.2 μm Radius of IRS 21

Date	Technique	# of frames	Radius ^a [AU]
1995 June	Speckle	800	680 \pm 70
1996 June	Speckle	600	760 \pm 170
1997 May	Speckle	900	750 \pm 130
1998 April	Speckle	588	790 \pm 115
1998 May	Speckle	980	900 \pm 90
1998 August	Speckle	980	700 \pm 40
1999 May	Speckle	1960	740 \pm 110
1999 May	AO	5	570 \pm 40
1999 July	Speckle	1370	680 \pm 90
<Speckle>			725 \pm 40
<Final>			650 \pm 80 ^b

^aRadii are estimated for the individual AO images and SAA images each of which is composed of 100 frames. Here we report the average and standard deviation of these estimates from each epoch.

^bThis size is the average of the radii estimated from the SAA and AO data and the uncertainty is the half-range of these values.

Table 2. Mid-infrared Radius and Flux of IRS 21

λ [μm]	Standard	PSF Star	θ_{PSF} ["]	Radius [AU]	A_λ^b	Total Flux ^c [Jy]	Flux-Background ^c [Jy]
8.8	IRS 7 & 3	IRS 3	0.59	<1830 ^a	2.5	3.21±1.9	1.34±0.8
12.5	α Boo	α Boo	0.31	1550±140	1.9	40.3±2.7	6.19±0.42
20.8	α Boo	α Boo	0.52	1480±200	2.0	58.0±17	3.70±1.10
24.5	α Sco	α Sco	0.61	1880±160	1.5	78.3±24	4.93±1.50

^aThis radius represents a 3 σ upper limit.

^bThe ISM extinction, A_λ , is derived from the extinction law of Moneti et al. 2001

^cObserved flux densities are within a 1''0 radius circular aperture.

Table 3. Best Fitting Parameters

Model	$\tilde{\chi}^2$	ρ_d 10 ⁻¹⁷ [g cm ⁻³]	T_{cen} [K]	R_{cen} [AU]	L_{cen} 10 ⁴ [L _⊙]	ρ_{NA} 10 ⁻¹⁸ [g cm ⁻³]	r_i [AU]	r_o [AU]
Constant	800	1.01	1000	17	1.2	...	500	...
1/r ²	80	0.12	980	20	1.5	0.95	780	1210
Bowshock	26	2.3	970	19	1.3	7.1	895	1800

Table 4. Properties of Stars with Luminosities of $10^4 L_{\odot}$

Type	Observed Properties			Modeled Properties ^a	
	L $10^4 L_{\odot}$	\dot{m}_*^b [$M_{\odot} \text{ yr}^{-1}$]	v_w^c [km/s]	$1/r^2 - \dot{m}$ [$M_{\odot} \text{ yr}^{-1}$]	bowshock - l [AU]
A5 I	3.5	1.96×10^{-7}	180^b	2.1×10^{-4}	70
G0 I	3.0	3.06×10^{-9}	160	2.0×10^{-4}	8
K0 I	2.9	4.22×10^{-7}	20	2.3×10^{-5}	33
K5 Iab	0.7	3.0×10^{-8}	60	7.2×10^{-5}	16
M1.5 I ^d	4.8	10^{-6}	17	2.0×10^{-5}	50
AGB ^d	0.6	10^{-5}	40	3.5×10^{-5}	735
WR ^d	3-100	10^{-6} - 3×10^{-4}	700-2500	8.1 - 30×10^{-4}	310-10,100
Ofpe/WN9 ^e	0.4-2.0	2 - 5×10^{-5}	400	4.7×10^{-4}	1270
WR WC9 ^d	28	10^{-5}	1000	1.2×10^{-3}	1160

^aModeled values are to be compared with observed values for \dot{m} (column 3) and size (~ 1000 AU). Those modeled properties which agree with the observations are in bold type. This rules out the mass-loss scenario and supports a bow shock model (column 6) for the last four entries.

^bLang (1997) unless otherwise noted

^cKudritzki & Puls (2000) unless otherwise noted

^dLamers & Cassinelli (1999)

^ePasquali et al. (1997)